JCIM JOURNAL OF CHEMICAL INFORMATION AND MODELING

Combining Deep Learning Neural Networks with Genetic Algorithms to Map Nanocluster Configuration Spaces with Quantum Accuracy at Low Computational Cost

Johnathan von der Heyde, Walter Malone,* Nusaiba Zaman, and Abdelkader Kara

Cite This: *J. Chem. Inf. Model.* 2023, 63, 5045−5055

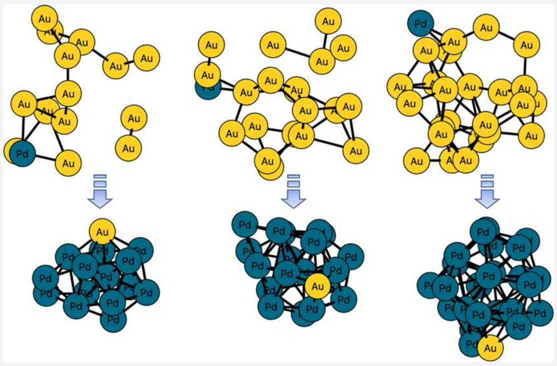

ABSTRACT: The configuration spaces for bimetallic AuPd nanoclusters of various sizes are explored efficiently and analyzed accurately by combining genetic algorithms with neural networks trained on density functional theory. The methodology demonstrated herein provides an optimizable solution to the problem of searching vast configuration spaces with quantum accuracy in a way that is computationally practical. We implement a machine learning algorithm which learns the density functional theory potential with increasing performance while simultaneously generating and relaxing structures within the system's global configuration space unbiasedly. As a result, the algorithm naturally converges onto the system's energy minima while mapping the configuration space as a function of energy. The algorithm's simple design applies not only to nanocluster configurations, as demonstrated, but to bulk, substrate, and adsorption sites as well, and it is designed to scale. To demonstrate its computational efficiency, we work with AuPd nanoclusters of sizes 15, 20, and 25 atoms. Results focus primarily on evaluating the algorithm's performance; however, several physical insights into possible configurations for these nanoclusters naturally emerge as well, such as geometric Au surface segregation and stoichiometric Au minimization as a function of stability.

1. INTRODUCTION

Machine learning (ML) has seen a large amount of success in the fields of physics, chemistry, and materials science predicting the properties of materials at the atomic scale. ML algorithms successfully predicted many properties such as molecular wavefunctions,[1] electron densities,[2] atomic charges,[3] bond order,[4] dipoles,[5] atomization energies,[6−8] excited states,[9] barrier heights,[10] adsorption energies,[11−14] and other properties.[6,9,15] ML predictions of these kind, while greatly accelerating the search for new, interesting compounds, do have drawbacks. First, ML methods require large datasets of either experimental or high-level theoretical calculations to train on, limiting the scope of these methods. Second, most ML methods are not fine-tuned to quickly calculate equilibrium configurations. Even with a neural network (NN) trained to predict forces and total energies, for example, one would still need to perform a single or several geometric optimizations if the system has a high entropy. We address these two problems by combining neural networks with a genetic algorithm (GA) to predict the local equilibrium and global minimum configurations of AuPd clusters with minimal DFT calculations.

AuPd clusters have been studied theoretically and experimentally as a model for heterogeneous catalysis and due to their catalytic properties.[16−23] A majority of these studies deal with experimental synthesis and characterization of AuPd nanoclusters.[16−20] In the group of Henry,[16−18] arrays of AuPd were synthesized on ultrathin films of alumina, ranging in size from a few atoms up to 400 atoms. These nanoclusters are tunable in size and composition and self-organize on the alumina substrates. Their stability at high temperature and under oxygen was established. Davis et al.[19] synthesized AuPd nanoclusters of sizes around 1 nm and characterized them with EXAFS. They found that Pd atoms decorate the core−shell nanoclusters of stoichiometry of $Au_{0.4}Pd_{0.6}$. They also reported a reduction of about 3% in the Au−Au nearest neighbor in the cluster, compared to Au-bulk. Theoretically, Shan et al.[21] used DFT-based empirical potentials (embedded atom method) to study AuPd nanoparticles of sizes ranging from 55 to 5083 atoms. They used a fixed shape (truncated octahedron) and five stoichiometries ranging from $Au_{0.1}Pd_{0.9}$ to $Au_{0.9}Pd_{0.1}$. The authors performed Monte Carlo simulations for these systems at different temperatures. They found that Au atoms decorated

Received: April 20, 2023
Published: August 14, 2023

https://doi.org/10.1021/acs.jcim.3c00609
J. Chem. Inf. Model. 2023, 63, 5045−5055

the smallest particles. For larger particles, Pd atoms are present at the skin of the cluster with an increasing concentration as the temperature increases. One of the very early DFT studies of bimetallic clusters at various stoichiometries[22] is on 33-atom CuAg nanoclusters. The study covers all stoichiometries from Cu_0Ag_{33} to $Cu_{33}Ag_0$ with varying shapes. This study showed that the HOMO−LUMO gap can vary substantially as a function of stoichiometry. They also reported a substantial reduction in the nearest-neighbor distance in the nanoclusters compared to their bulk counterparts. More recently, Zaman et al.[23] used DFT to study a variety of bimetallic nanoclusters of a fixed size of 5 atoms. They investigated Pd_3M_2 (where M = Ag, Au, Co, Cu, Mn, Ni, Pt, and Ru) clusters on the hydroxylated alumina surface. They focused on the gap between the top of the valence band and the fermi level and found that this quantity can be tuned by varying the chemical entity of the M guest atom.

More generally, AuPd alloys have been demonstrated to effectively catalyze several reactions: CO oxidation,[24,25] vinyl acetate synthesis,[26] and aromatics hydrogenation.[27,28] Nanoclusters are broadly attractive as catalysts because one can fine-tune their reactivity for given applications.[29] Indeed, this is the main reason we chose to study AuPd nanoclusters here. By selecting for particle size, composition, and stoichiometry, one gains a high level of control over the chemical properties of the nanoparticle. However, finding the most stable nanoparticle configurations that will form under reaction conditions is challenging to predict due to the enormous configuration spaces available to such systems.

As such, there is a growing need for computational methods that can search the vast configuration spaces available to nanoclusters, substrates, adsorption sites, etc., such that unique states and global patterns can be identified efficiently. To understand the size of these spaces, consider an icosahedral cluster of 13 atoms (one in the core and 12 evenly distributed around). We have n^{13} possible states, where n is the number of unique elements comprising the cluster substrate (each of the 13 spaces will have n elemental options)—e.g., Au_nPd_m (where $n+m = 13$) has two elements, and so there are $2^{13} = 8192$ states. Even if we restrict ourselves to a certain stoichiometry, e.g., Au_6Pd_7, we get 13 choose 6, which makes for 1716 possible states. This assumes that the symmetric states can be distinguished (ordered combination), but it also severely limits the actual geometries available to such clusters. *In situ*, we are rarely dealing with such high symmetries, and indeed, clusters and substrates naturally tend to organize themselves in local not global minima. Therefore, the number of possible configurations for similar systems makes them impossible to evaluate with high precision in reasonable time. Moreover, once we open the door to undefined configurations, compositions, and stoichiometries (also known as high-entropy states), any method of "brute-force" exploration quickly becomes intractable, hence the demand for sophisticated search algorithms to explore and map these vast state spaces.

Performing all of the calculations needed to completely map configuration spaces of this size would be impossible, even with a neural network (NN) or similar ML method alone. This requires accurately and precisely predicting energies and forces while also performing the necessary geometry optimizations. To further streamline the process then, we utilize a GA[30,31] for the global minimization process. A GA can change the structure of molecules and materials according to some predetermined fitness criteria. In our case, the fitness function is a measure of a lower total energy. Therefore, our GA will continuously modify, mix, and filter clusters while searching for the lowest energy configurations in an otherwise unbiased, stochastic fashion. And instead of direct DFT calculations, this fitness function is calculated 3−4 orders of magnitude faster using an NN trained on energies and forces. Here, we chose to optimize the ML algorithm with cluster total energy as the GA's fitness function; however, we could have chosen atomization energy instead. While the overall performance of the algorithm is independent of this difference, we recognize that the GA will converge onto different structures depending on the fitness function's definition, and therefore, one would expect to end up with different structures within a different global minimum—some analysis of total energy vs atomization energy is explored in Section 3.

GAs have a long history in the field of chemistry and physics. A combined DFT-GA approach has been utilized to study metallic nanoclusters on surfaces[32,33] and in vacuum.[34−40] Paleico et al.[32] explored clusters of copper atoms, from 4 to 10 atoms, adsorbed on a $ZnO(10\bar{1}0)$ surface utilizing an NN and a GA with DFT reference data. Their NN predicted energies which the GA used to evaluate fitness. The GA employed direct, large-scale modification of the atomic coordinates of the cluster such as mirroring through a plane. Overall, they reported that clusters tend to prefer to interact with the surface through the O atoms. Heydariyan et al. utilized a GA in tandem with density functional tight binding to study Si clusters ranging from 8 to 80 atoms in size. In addition to finding previous unreported clusters, they noticed a transition at 27 atoms from elongated to globular structures.[35] Seifried et al. employed a GA to predict the most stable Pb_nBi_{13-n} clusters in tandem with aimed swapping of element types by perturbation theory in nuclear charge.[40] This method,[41] known as "alchemical derivatives,"[42,43] can save time over using only DFT. However, it requires the two elements in the cluster to have similar nuclear charges.

In our approach, we study the configuration space of AuPd clusters while generating our own DFT reference data as a validation step, during self-optimization. These configuration spaces are explored automatically via a series of global iterations as the ML algorithm descends the configuration space, improving upon its training data and in-turn improving its predictive performance, significantly reducing the computational cost compared to traditional approaches. Our approach is demonstrated to work with clusters with two different elements yet can generalize to high-entropy systems. In Section 2, we discuss our methods, in Section 3 we present our results, and in Section 4, we present our conclusions.

2. METHODS

We consider this an open-ended optimization problem, wherein the task is to map the system's physical properties as a function of configuration, for a domain-specific set of atomic (elemental composition and stoichiometric variability) and geometric constraints. Specifically, we demand state-of-the-art energy and force calculations typically provided via DFT. Since these calculations are as precise as they are slow, despite being parallelizable, many have turned to NNs to try and model the DFT functional for various systems.[1−9,15] A DFT-trained NN has the advantage of being able to accurately predict atomic properties several orders of magnitude faster than DFT. However, training these NNs typically requires many DFT calculations regardless. We optimize this process by

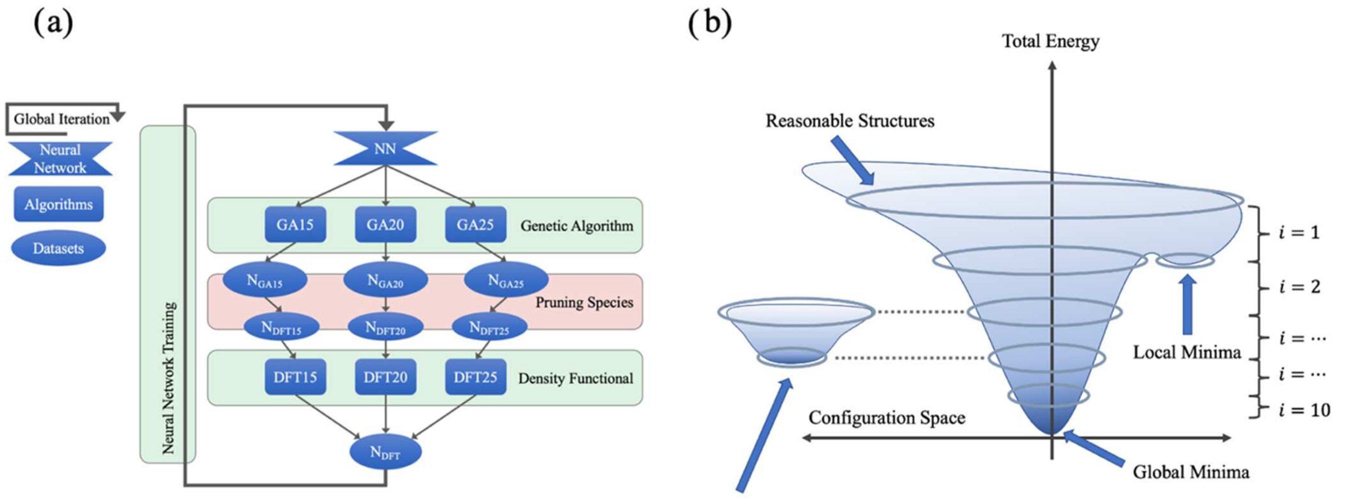

Each iteration's images lie on the surface of a slice of possible structures within the defined cluster's own reasonable configuration space.

Figure 1. (a) Algorithmic schema: DFT-trained NN (top) evaluates structures generated by the GA (unique to each cluster size and stoichiometry), which are then pruned down to uniquely representative structures for that iteration's slice of the configuration space (see panel (b)), then validated by 1 ionic DFT relaxation, and finally included into the next iteration's training data (bottom). (b) 2D visual representation of a configuration space as a function of cluster total energy. "Reasonable structures" are those satisfying our atomic and geometric criteria, and they lie on a hypothetical surface where proximity is a function of atomic and geometric similarity. Our algorithm descends this possibility space automatically and maps structures within each iteration's sampling range along its way toward the global minima.

generating our own training data automatically, which is applicable for situations where high-level training data is not available. Moreover, we train our NNs exclusively on *uniquely representative* (UR) structures—this means minimizing the amount of DFT validation calculations required to build a robust network. UR structures are defined as those which pass two filters: First, cluster energies must be unique up to 1 meV—this parameter value minimizes our system's cluster degeneracy while preserving geometric nuance. Second, each atom's forces must be less than two standard deviations away from that of their cluster—this safely removes unrealistic configurations, where, for example, atoms may be on the verge of breaking off the cluster, while preserving transition states. Symbolically, uniquely representative (UR) structures can be defined as

$$UR = U \cap R \tag{1}$$

$$U = |i - j| > 0.001eV \ \forall \ i, j \in E \tag{2}$$

$$R = ((i < 2\sigma) \ \forall \ i \in f) \ \forall f \in F \tag{3}$$

where E is the set of energies per cluster, f is the set of forces per atom (xyz), and F is the set of forces per cluster. Note that these filtration parameters are system-specific.

The key insight into developing our ML algorithm is to combine DFT accuracy, NN speed, and the GA search by letting DFT-trained NNs serve as the fitness functions for our GAs. To search the configuration spaces, many options are available; however, GAs have proven especially useful for our purposes, given their tunable preference for exploration and exploitation.[30,31,44] They are modeled after biological evolution by natural selection and serve us by generating "fit" structures within our constraints with minimal bias, based on selective mixing and mutation procedures. In recent works, GAs have been combined with NNs,[45−47] as well as with DFT.[48−50] As such, our ML algorithm generates structures with DFT-accurate properties, via the GA, which are then filtered (or "pruned") for validation by minimal DFT calculations and fed back into the NN for further training. This process can be iterated in an intuitive way via a global feedback-loop and will converge naturally on the global energy minimum once the reasonable configuration space is sufficiently mapped (see Figure 1). The term "reasonable" reflects our domain-specific geometric and atomic constraints (such as the cell size, minimal interatomic distance, and stoichiometry); we do not claim to map the possibly infinite state space available to such systems.

In more detail, our GA is built as a customization of the atomic simulation environment[51] GA. It is designed to filter unreasonable structures upstream via a simple linear regression estimator on the energies, saving some computation time and allowing a reasonably high mutation probability of 0.3. The initial population consists of 100 structures which go on to evolve into 1000 structures, per stoichiometry, per cluster size. The GA is interfaced with a deep, continuous filter, convolutional neural network, as parameterized from SchNetPack[52] trained on modern GPUs with CUDA,[53] such that it can quickly and accurately evaluate a given cluster's fitness as its total energy, relative to the given population. Once filtered, these structures are validated and relaxed via DFT. These simulations are externalized from Python, such that they may be more easily parallelized via the Vienna Ab initio Simulation Package[54−56] on a large compute cluster. We use the GGA functional from PBE,[57] with the PAW[58] method, run for a single ionic relaxation with a minimal energy difference of 1E-5 eV (EDIFFG tag), which translates to 50−100 electronic loops per cluster. These DFT images are then used for training the next iteration's NN. We use an energy/force loss ratio of 0.1 to emphasize force-training 10-fold, and a cutoff of 5 Å, trained for a maximum of 500 epochs on ~300 additional clusters per global iteration (100 per cluster size), with training/validation/testing split percentage of 80:10:10 and a minimal learning rate of 1E-4, where loss is calculated as the mean absolute error (MAE) of the validation set.

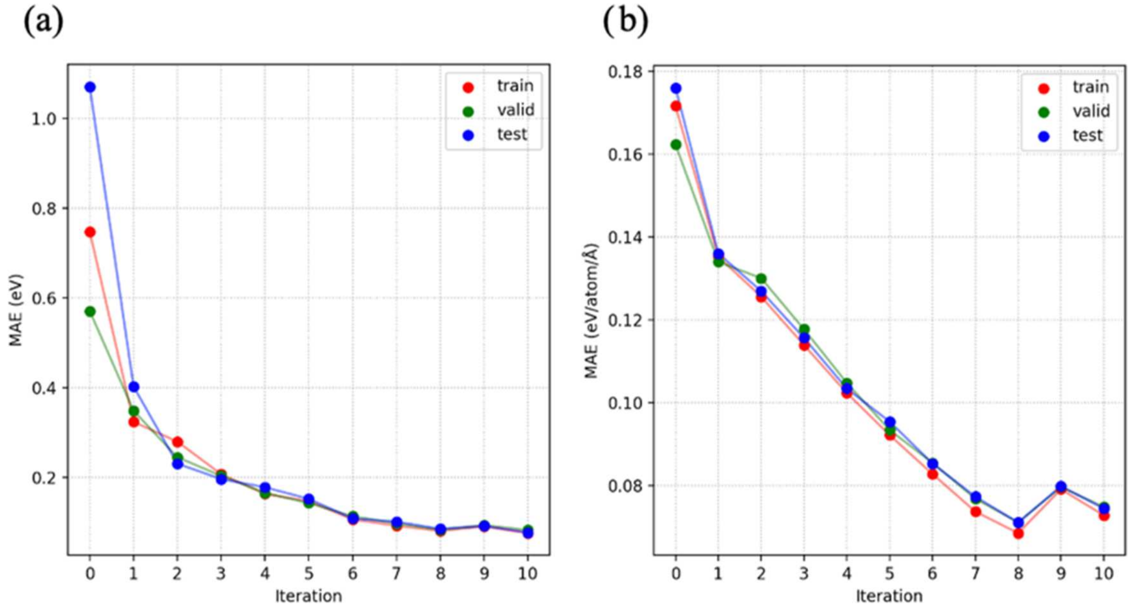

Figure 2. Mean absolute error (MAE) for energy predictions (a) and force predictions (b) for all clusters trained upon during each global iteration. Note that forces are calculated per atom, per dimension (*xyz*), unlike energies which are calculated per cluster unless otherwise stated.

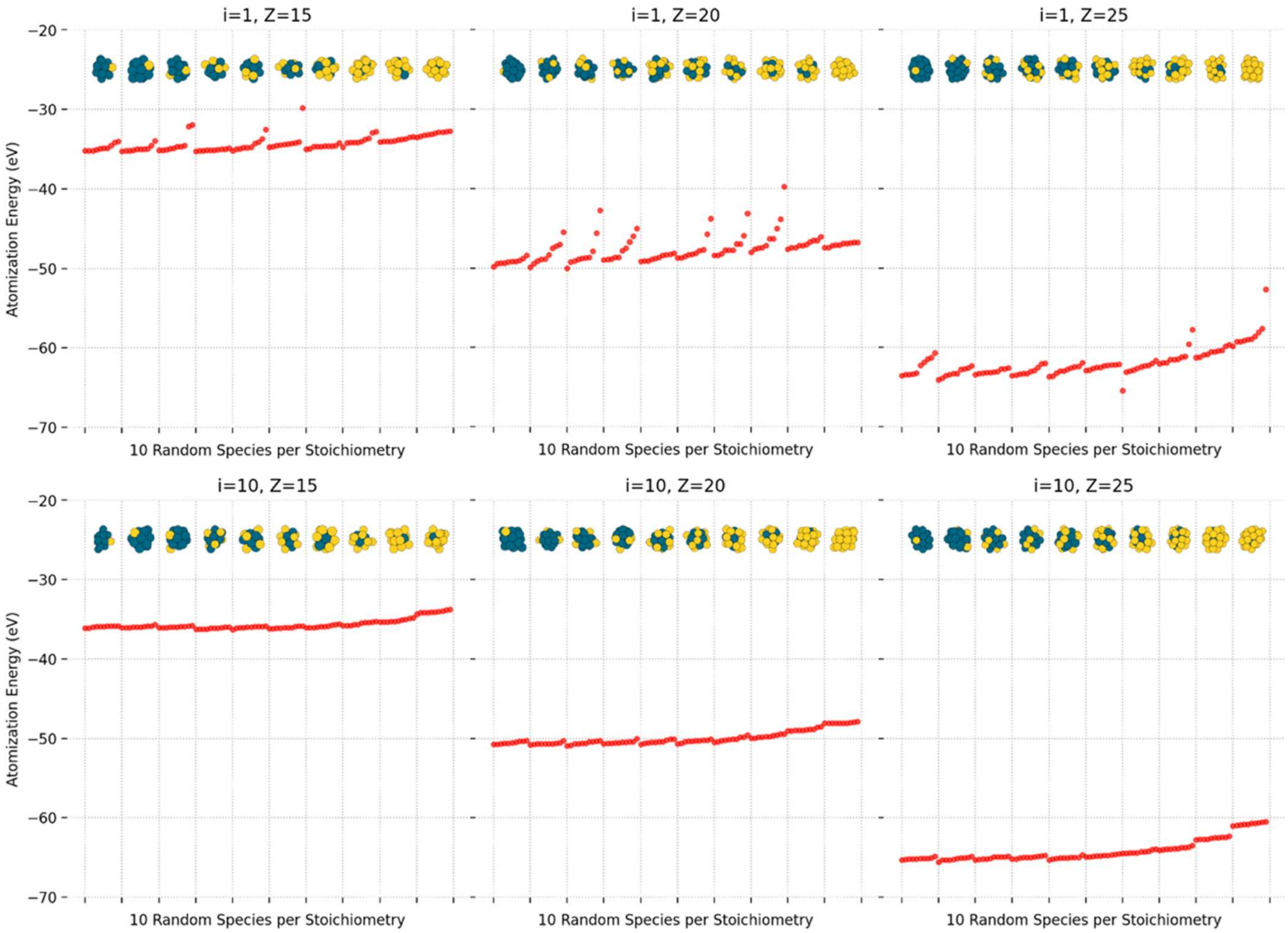

Figure 3. Cluster atomization energy as a function of stoichiometry. 10 random clusters sampled from 10 evenly distributed stoichiometries shows 100 structures organized from Au_1Pd_{N-1} to $Au_{N-1}Pd_1$. The first row shows the 1st global iteration, and the second row the 10th, while each column shows each cluster size separately.

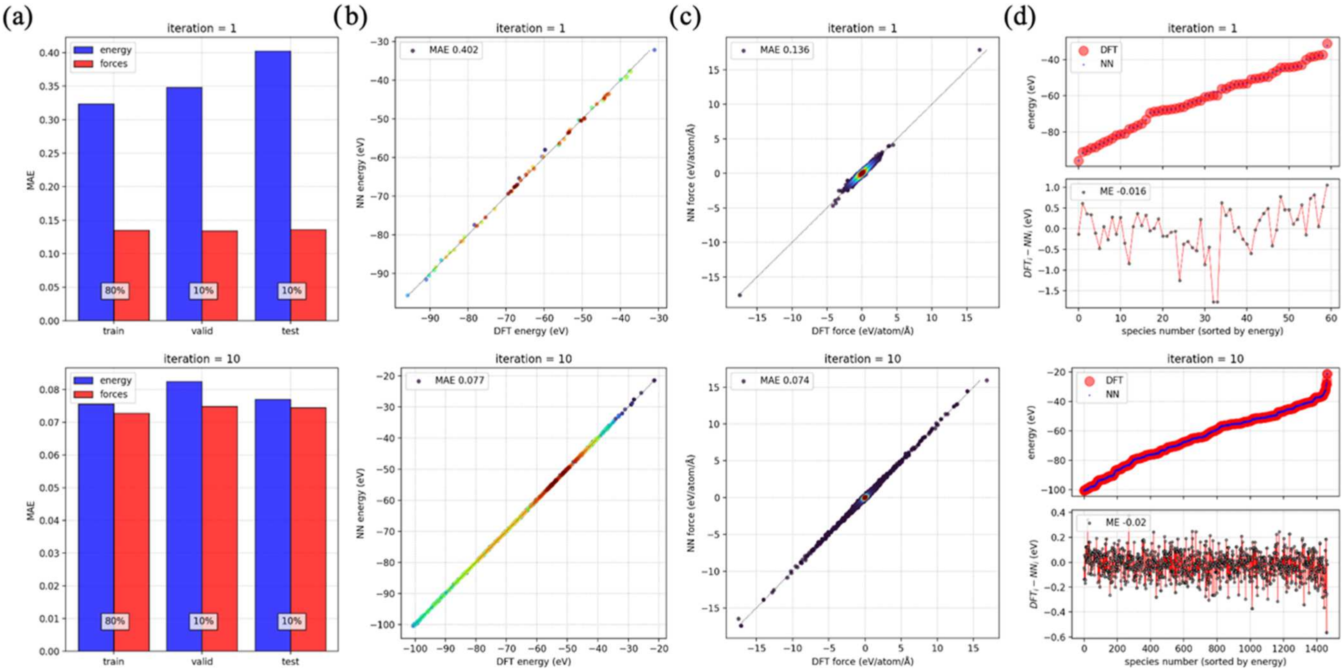

Figure 4. Explicit internal energy and force plots, comparing predictions (NN) with reference (DFT) for the 1st and 10th global iterations. Panel (a) shows train−valid-test data split, along with the corresponding split percentages (note that here the y axis MAE implies units of eV for energy and eV/atom/Å for forces). panels (b) and (c) showcase the energies and forces, respectively, whereas panel (d) shows the signed (as opposed to absolute) difference between DFT reference and NN predictions as organized by total energy.

The ML algorithm has been specifically tailored to the demonstration of AuPd nanoclusters of sizes 15, 20, and 25 atoms—its general schema is shown in Figure 1. N_{GA} clusters of each size are generated by their own GA (with multiple stoichiometries each) and pruned into a set of UR clusters for relaxation in DFT, out of which comes N_{DFT} clusters, which are added to the training set for the next iteration's NN. In Figure 1b, we see cluster energy as a function of the reasonable configuration space. Our ML algorithm will naturally descend this abstract surface due to the GA's fitness function being a measure of cluster total energy (note that this is a visualization of what the configuration space as a function of energy might look like and is not meant to be taken literally). This, coupled with relaxation steps, as performed via the NN within the GA (BFGS algorithm), ensures that the algorithm will converge automatically when it has run out of UR structures to generate, and NN loss plateaus. Each global iteration, seen as one whole loop within Figure 1a, samples a local slice of the reasonable configuration space such that the algorithm can map local minima during global descent—this local exploration, within the global optimization, helps to ensure that we do not miss unique states.

Seed data is required to start the ML algorithm, and for this system, only ∼300 UR structures within the search space are needed (number being domain-specific) and were generated via a GA and relaxed in DFT. Once the initial NN has been trained, the main programmatic loop can begin. Here demonstrated, each GA generates 500 structures per 10 stoichiometries, per cluster size, and out of these 15,000 "images," only about 2% survive the pruning process, go on to be validated in DFT, and train the next NN. Note that while this may seem like a waste of computation, most of the state space is symmetrically degenerate, i.e., uninteresting, and most of the computation is done via the NN within the GA, which has its own methods to avoid wasting computation on unreasonable structures as mentioned earlier, and so generating 15,000 structures takes <1 hr if parallelized.

This methodology also provides an option: One can either continuously build upon a single cumulative NN during global optimization or train a NN specific to each global iteration. We found the results to be similar, yet here made each global iteration's training data cumulative, such that the NN for each iteration uses its knowledge of previous iterations to better predict images in the next local slice of reasonable configuration space (Figure 1b). This makes for slower algorithmic convergence (more time spent training) yet better performance. Additionally, it might be convenient for one to use a more sophisticated pruning method—such as emphasizing clusters the NN has trouble with or, contrariwise, those that it did well to predict. This choice is analogous with that of exploitation vs exploration in machine learning, and we have chosen the simple method of UR images as a balanced compromise, which we found to optimize the ML algorithm's performance overall. Indeed, one should not expect global monotonic improvement in predictions if one is emphasizing training on challenging images, and if one is emphasizing images the NN predicted well, the ML algorithm could orbit local rather than global minima.

3. RESULTS

Our main result is the ML algorithm's performance as measured by its ability to improve DFT predictions as it maps its way down the reasonable configuration space, as shown in Figure 2. If not otherwise stated, we are using MAE to quantify performance, which is determined by the mean absolute difference between DFT reference values (energies and forces) and the NN's predictions. Typically, the total energy is what is calculated, although, in Figure 3, we analyze the atomization energy instead. We conclude that within these

Table 1. Consistency Measures for the Cumulative Neural Network (Iteration 10)

cluster sizes	15, 20, 25		inner (16−19, 21−24)		outer (11−14, 26−29)	
generation method	internal	external	external GA	external MD	external GA	external MD
energy MAE (eV)	0.074	0.212	0.264	0.258	0.337	0.332
energy MAE (eV/atom)	0.004	0.011	0.013	0.013	0.020	0.021
force MAE (eV/atom/Å)	0.070	0.117	0.146	0.190	0.149	0.196
max energy error[a]	0.679	1.095	1.762	1.731	2.013	1.995
max force error[a]	0.967	1.240	3.032	2.236	2.890	2.224
test set sample size	1500	1500	500	800	500	800

[a] Units here for energy and forces are eV and eV/atom/Å, respectively. Explicit plots for these values are given in the Supporting Information (Figures S1 and S2).

domain-specific criteria, as well as our hyperparameterization, that only ∼8 global iterations are required to map all UR structures within this space. Convergence is seen as the point at which the ML algorithm fails to improve over some iterations, which is consequent to a lack of novel structures being generated. Here, it is seen that after 8 iterations, MAEs bounce around 0.07 eV/cluster for energy prediction and 0.06 eV/atom/Å for force prediction, without significant changes—analogous to oscillating about the bottom of the global minima. We take the monotonic improvement in our DFT predictions as a function of global iteration to be consequent to a shrinking state space, as well as hyperparameter optimization. To avoid overtraining or to improve prediction generalizability beyond the training data's domain, one may choose to interrupt the global convergence earlier.

Clusters generated by the algorithm, as seen from the 1st and 10th global iterations, are plotted in Figure 3 (Au is colored gold, and Pd is teal). These are DFT energies and geometries, which would go on to train the corresponding iteration's NN. They contain an even distribution of UR samples from 15-, 20-, and 25-atom clusters. As such, one can witness the energetic "steps" form as the NN learns the important differences between cluster size, stoichiometry, and stability. A smooth transition between a noisy broad distribution (iteration 1) and a uniform stepped distribution (iteration 10) is essential to demonstrate that our algorithm learns not only these clusters but is also capable of inferring the sizes and stoichiometries between them as well, as tested. Moreover, it is immediately obvious that cluster atomization energy is weakly correlated with Au occupation—that is, the more Au in a given cluster, the weaker (less negative) the atomization energy. Moreover, this relation is somewhat trivial for cluster total energy because a single Au atom's total energy is considerably less negative than a single Pd atom's total energy as calculated by DFT (−0.135 and −1.473 eV, respectively), and so for clusters of similar relaxed geometries, the stoichiometry heavily determines its total energy with the subtle differences in geometry playing a smaller role. However, the fact that this relationship is still present, to some degree, with respect to atomization energy indicates that it is a much more meaningful relationship.

Energy and force predictions are made on test data set aside from training and validation data of each global iteration. Figure 4a shows these results for the training, validation, and testing data separately, whereas Figure 4b−d shows just the testing data which the NN never sees—yet which are sampled from each iteration's UR structures. The color in Figure 4b,c reflects a Gaussian kernel density estimation (KDE) and so is normalized from blues (low density) to reds (high density), with Scott's rule for covariance factor. This makes it obvious to see exactly what the NN is predicting. For example, beyond the spreading of energies by cluster size, as seen in the bottom plot (Figure 4b), we also see how most all of the forces have begun to accumulate around zero (Figure 4c) as more clusters converge within the global minima. In Figure 4d, we plot the energy landscape at the top and below the direct energy prediction errors for each species as DFT_i-NN_i (positive and negative), where it is shown that the NN overestimates about as much as it underestimates, with even the most outstanding errors well within 1 eV per cluster for all three sizes.

Next, we evaluate the ML algorithm's cumulative NN against external cluster sizes which it has never seen. We define two sets: "inner" cluster sizes between but not including 15, 20, and 25 atoms and "outer" clusters from 11−14 atoms and from 26−29 atoms. This way we can separately test the NN's performance on larger and smaller clusters, as well as those within and outside its training data range separately. We do so via two distinct generation methods (with GA and MD)—see Table 1 for these details, where values are also scaled by cluster size for better comparison.

"Internal" images are those sampled from training databases—be they from training, validation, or test sets, which serves as a randomized metric for self-validation. "External" images are generated completely separately from the ML algorithm, which allows us to test the NN's predictions on sizes and stoichiometries it has never seen. MD images are initially generated by a GA yet are then coupled to a simulated heat-bath of 1000 K and iterated under Langevin dynamics, with a time step of 10 fs and a friction coefficient of 0.002 Hartree/$\hbar$. This allows us to test the cumulative NN against novel configurations the GA might not generate with more realistic forces. To see the NN's prediction on specific cluster sizes, please refer to Figures S2 and S3 in the Supporting Information. What we find is that the NN predicts more or less evenly across inner and outer clusters alike, which is proof of its ability to generalize the system state space, yet it is of course better at internal images of its own training sizes. For external images, it is slightly better at predicting the MD energies compared to GA energies, yet slightly worse at MD forces compared to GA forces. This is probably due to the fact that the MD simulations tend to give symmetric energy distributions, while simultaneously adding new asymmetric forces.

To further determine the nature of these errors, we analyze cluster stability as a function of stoichiometry. This is important because we have yet to determine how the prediction errors relate specifically to each element within the cluster. To test this, we examine the middle NN's performance (iteration 5), in predicting cluster energies specifically as a function of Au percentage. We use the 5th

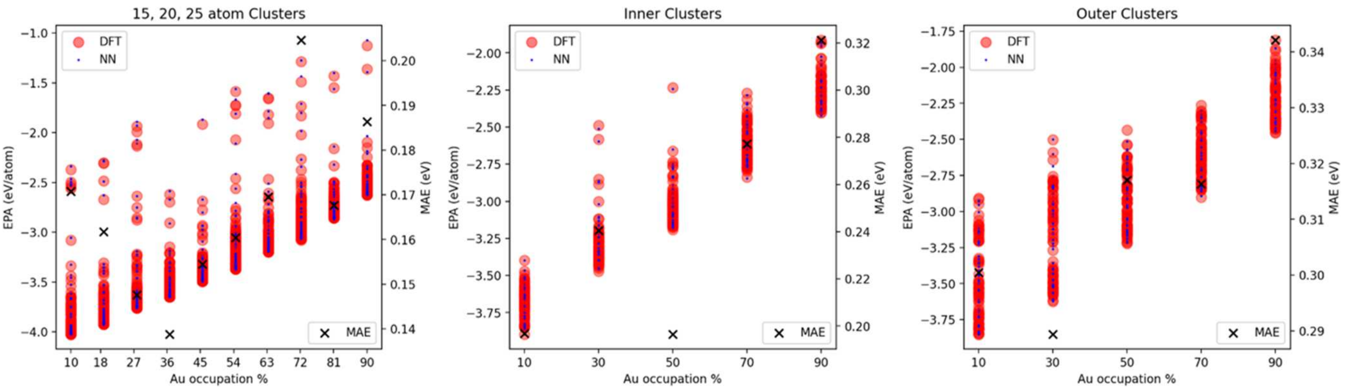

Figure 5. Cluster stability and NN performance as functions of Au occupancy. Au % ranges from 10−90, with 10 evenly spaced stoichiometries for 15-, 20-, and 25-atom clusters, consisting of 80 random samples each, and 5 evenly spaced stoichiometries for inner and outer clusters, consisting of 10 random samples each. Like Figure 4d, red circles are DFT reference energies and blue dots are the associated NN predictions. Additionally, for each stoichiometry, we have MAE values indicated by black x's, taken over all cluster sizes.

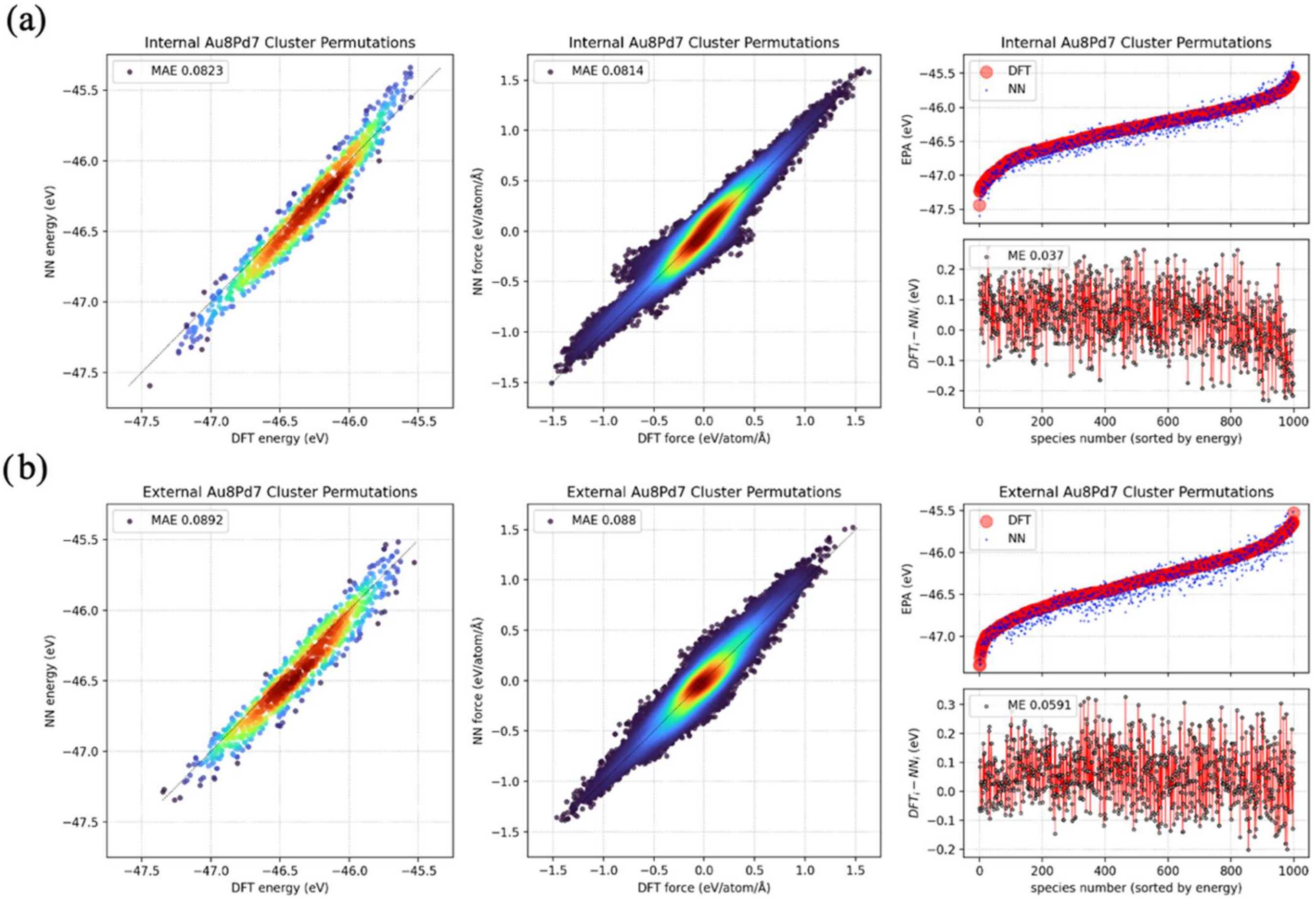

Figure 6. Two random, mostly relaxed Au8Pd7 geometries. One taken from datasets internal to training (a) and one from datasets external to training (b). For each, 1000 out of the total 6435 possible permutations were randomly sampled. Occupancies were then relaxed for one ionic loop in DFT, and the plots show the NN prediction errors by comparison. From left to right, we see energy and force MAEs, followed by energy mean error (ME).

NN to minimize bias toward 15, 20, and 25 atoms, as it was found that beyond iteration 5, predictions improve for those sizes yet slightly worsen for inner and outer clusters—which could be interpreted as overtraining if the desire is to generalize rather than specialize the NN. These results are shown in Figure 5. For 15-, 20-, and 25-atom clusters, we have 10 evenly distributed stoichiometries to work with, ranging from 10% Au, 90% Pd to 90% Au, 10% Pd. Within each of these stoichiometries, we randomly sample 80 clusters, for each cluster size. The DFT reference energies (red circles) are plotted on the left axis, along with the associated NN predictions (blue dots). The MAE values across all cluster sizes for each stoichiometry (black x's) are measured on the right axis. The only difference for inner and outer clusters is that we just have 5 stoichiometries to work with, out of which we only pull 10 unique clusters, again for each cluster size.

Table 2. Elapsed Wall Times for DFT and NN Calculations as Averaged over ∼1000 Cluster Images[a]

types of computation	time (s)	15-atom clusters	20-atom clusters	25-atom clusters
DFT (1 ionic iteration)	min	1.467×10^{2}	1.028×10^{2}	1.974×10^{2}
	mean	3.696×10^{2}	2.427×10^{2}	5.016×10^{2}
	max	2.545×10^{3}	1.725×10^{3}	1.982×10^{3}
NN (calculate energy and forces)	min	2.435×10^{-2}	2.831×10^{-2}	3.435×10^{-2}
	mean	3.582×10^{-2}	4.495×10^{-2}	5.431×10^{-2}
	max	5.870×10^{-2}	7.127×10^{-2}	7.267×10^{-2}

[a] Note that some DFT calculations can stall for an unexpected amount of time, as seen in the maxima; however, such anomalies fail to account for the widespread difference in DFT and NN runtimes.

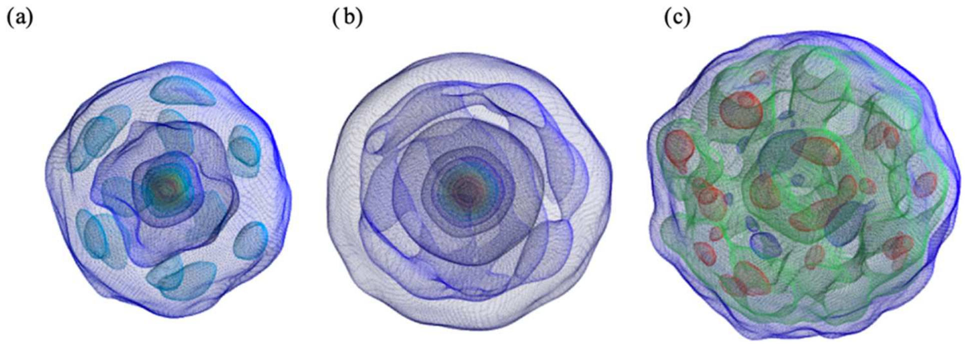

Figure 7. Gaussian kernel density estimations for atomic positions over ∼1000: (a) 15-, (b) 20-, and (c) 25-atom clusters. We use 5−7 contours to help distinguish the extra nuance in configurations associated with larger clusters (Scott's factor for covariance).

These plots reveal something very interesting: prediction errors are indeed a function of Au %, yet the relationship is nonlinear. As seen in Figure 3, we already know Au % is a strong linear predictor of AuPd cluster total energy; however, now we can see exactly how this translates to errors in the NN prediction. Figure 5 thus provides evidence for the source of MAE errors being correlated, but not fully explained, by cluster total energy—note that since a consistent conversion between cluster total energy and cluster atomization energy is always possible, the MAE prediction errors are not affected by this choice. Moreover, by simply "flipping" the stoichiometries of a sample of clusters (swapping Au for Pd and vice versa) and validating them with DFT, we can directly test if our NN has any bias toward either stoichiometric distribution. This examination is provided in Figure S3 in the Supporting Information, where minimal statistical bias was found.

We conclude that our MAE prediction errors must then be correlated not only with stoichiometry but also more subtly with occupancy (which atom is in which geometric position within the cluster), for there is no other variation present in the training data distribution. Therefore, we are motivated to test the NN's precision in evaluating the subtle differences in cluster energy when varying the exact occupancy of the stoichiometric distribution. For this test, we select just two clusters of 15 atoms of mostly even stoichiometric mixture Au_8Pd_7, one internal to the training data and one external to the training data—both of which are almost totally relaxed with DFT. We hold constant the geometry and permute over its occupancy, which would generate 15 choose 7 or 8, i.e., 6435 clusters each. From these possibilities, we take a more pragmatic random sample of 1000 clusters and compare DFT vs NN predictions for these cluster permutations. Results are shown in Figure 6. We found that in this high-demand precision test, the final NN has trouble differentiating the subtle energetic differences for the cluster occupancies and likely estimates its energy based on the most similar stoichiometry it has seen, leading to slight yet consistent over- and underestimations of cluster total energy.

In an effort to be thorough, we also relax in DFT the "top-10" most stable UR structures for each cluster size for a total of 10 ionic steps and compared the final energies and forces with what the cumulative NN would have predicted after 10 relaxation steps of its own, using the BFGS algorithm. Results of which are in Figure S4 in the Supporting Information (geometries shown in Figure S5) and showcase very similar predictions for 25-atom clusters and even better predictions for 15- and 20-atom clusters. This demonstrates that the NN knows not only the energy and forces of structures within the system's configuration space but can also reliably relax such structures just like DFT.

Whereas Table 1 analyzes accuracy, Table 2 showcases how fast the NN is compared to DFT—roughly four orders of magnitude in general. DFT times shown here do more than calculate energies and forces; however, as they are initialized by VASP, many subprocesses must occur before electronic and ionic iterations begin. Nevertheless, this difference fails to compare with how much faster the NN is. Of course, we also have to train the NNs which occupies a fair amount of the total global iteration runtime, yet using the NNs in this fashion is exactly what enables the GA to search such a vast configuration space with high accuracy in a very reasonable amount of time—trying to generate the same structures with the GA by using DFT instead of the NN for force and energy calculations would take thousands of hours.

One natural result of mapping global configuration space is the statistical accumulation of clusters into regimented patterns—geometric phases. These can be identified with some post processing as seen here in Figure 7. This maps the probability density of positions within the set, using another gaussian KDE. Here, we took ∼1000 DFT images from the final global iteration's training data for each of the 3 sizes. In Figure 7, we see for 15-atom clusters, mostly every morphology is based upon the 13-atom icosahedron (one atom in the core and 12 evenly distributed outside), with extensions added on rather arbitrarily. Yet for 20-atom clusters, there is no regimented pattern preferred, only layers of nearest-neighbor occupations, and so morphology tends to represent radial stochastic clumps. The same is true for 25-atom clusters; however, now the layers outside the core are just as occupied as the core itself, representing a transition toward bulk morphology.

Another natural consequence of this global optimization scheme is that core−shell segregations become apparent. Here, the ML algorithm tends to minimize Au as it descends the energy landscape due to the Pd−Pd bonds being stronger than Au−Pd and Au−Au bonds. During this process of Au minimization, we see a natural core−shell segregation, with Au moving to the surface of clusters and Pd moving to the core (see Figure S6 in the Supporting Information). This is found to be true for atomization energy and total energy, although clusters with minimal atomization energy will not necessarily minimize Au as is in the case for total energy. Furthermore, this is seen more explicitly as first- and second-neighbor coordination distributions in Figure S7 in the Supporting Information. These physical insights can be used to guide the fine-tuning of electronic properties, which is highly desirable for applied nanocluster research.

4. CONCLUSIONS

We have demonstrated how state-of-the-art deep neural networks can be utilized to estimate DFT energies and forces precisely and accurately (for over 99% of clusters tested) with bimetallic clusters of sizes 15, 20, and 25 atoms, regardless of stoichiometry, and how combining these NNs with GAs allows one to generate stable clusters within the local configuration space. Combining these two facts together allows us to construct an ML algorithm capable of mapping the system's configuration space as validated by DFT, which automatically converges to the bottom of the system's energy minima. The optimization of such an algorithm only requires minor domain-specific hyperparameterization as well as an efficient method for pruning "uniquely representative" structures. Whereas NNs have been trained on DFT images in the past, and GAs have been utilized in conjunction with DFT, the combination of all three methodologies into one optimization program is to our knowledge new.

This optimization minimizes actual DFT calculations. For example, with just 10 global iterations, we generate ∼9,000 DFT-accurate configurations (3 sizes × ∼300 UR structures × 10) in about 20 hours ((∼0.1 h DFT + ∼1 h GA + ∼1 h NN training) × 10). Moreover, these 9000 configurations automatically represent unbiased samples across the global configuration space, thanks to our UR pruning method and the GA's intrinsically unbiased stochastics. Beyond minimizing DFT calculations, we also attempt to maximize the domain of the cumulative NN's applicability—including cluster sizes and stoichiometries outside its training set with minimal loss in predictive power (∼0.3 eV MAE for all cluster sizes and stoichiometries tested). This also necessitates the avoidance of overtraining, whereby the more precisely the NN can predict the trained sizes, the less precisely it can predict sizes outside of its training domain—such a tradeoff is inevitable; however, the overall performance of the NN predictions can always be improved with more data and more sensitive hyperparameter values.

In general, the ML algorithm here demonstrated serves as a pragmatic solution to the problem of mapping large atomic state spaces with quantum accuracy without a large amount of computation time. Such a simple DFT+GA+NN methodology can be easily extended to bulk, surface slab, and adsorption site exploration as well (results of which are left to future reports), especially in situations where one lacks labeled reference data to begin with. This research's application starts with new, pragmatic methods in computational physics and spreads to more specified theoretical domains, specifically catalysis design and materials discovery, with the simple introduction of domain-specific parameterization. Further research will explore high-entropy structures of various composition and stoichiometry, revealing in practical computation, unique states amid vast possibilities for the growing experimental interest. As neural networks have been demonstrated to predict well on larger clusters and different bimetallic and high-entropy metallic clusters, we anticipate a high level of transferability for this methodology.

■ ASSOCIATED CONTENT

Data Availability Statement

Datasets utilized in this manuscript are available in the Supporting Information. The genetic algorithm coupled with the neural network code is available under MIT license on GitHub: https://github.com/anywallsocket/Professional-Projects

Supporting Information

The Supporting Information is available free of charge at https://pubs.acs.org/doi/10.1021/acs.jcim.3c00609.

> Supporting Information contains explicit neural network performance evaluations (S1−S3), neural network-based relaxation tests (S4), and various geometric calculations (S5−S7) (PDF)
>
> Full cluster datasets along with smaller datasets containing our lowest total energy structures (ZIP)

■ AUTHOR INFORMATION

Corresponding Author

Walter Malone − *Department of Physics, Tuskegee University, Tuskegee, Alabama 36088, United States;* orcid.org/0000-0001-8245-322X; Email: wmalone@tuskegee.edu

Authors

Johnathan von der Heyde − *Department of Physics, University of Central Florida, Orlando, Florida 32816, United States*

Nusaiba Zaman − *Department of Physics, University of Central Florida, Orlando, Florida 32816, United States*

Abdelkader Kara − *Department of Physics, University of Central Florida, Orlando, Florida 32816, United States;* orcid.org/0000-0003-1445-1315

Complete contact information is available at: https://pubs.acs.org/10.1021/acs.jcim.3c00609

Notes

The authors declare no competing financial interest.

■ ACKNOWLEDGMENTS

Walter Malone acknowledges support from the National Science Foundation RISE Grant #2122985.

REFERENCES

(1) Schütt, K. T.; Gastegger, M.; Tkatchenko, A.; Müller, K.-R.; Maurer, R. J. Unifying Machine Learning and Quantum Chemistry with a Deep Neural Network for Molecular Wavefunctions. *Nat. Commun.* **2019**, *10*, 5024.

(2) Grisafi, A.; Fabrizio, A.; Meyer, B.; Wilkins, D. M.; Corminboeuf, C.; Ceriotti, M. Transferable Machine-Learning Model of the Electron Density. *ACS Cent. Sci.* **2019**, *5*, 57−64.

(3) Nebgen, B.; Lubbers, N.; Smith, J. S.; Sifain, A. E.; Lokhov, A.; Isayev, O.; Roitberg, A. E.; Barros, K.; Tretiak, S. Transferable Dynamic Molecular Charge Assignment Using Deep Neural Networks. *J. Chem. Theory Comput.* **2018**, *14*, 4687−4698.

(4) Magedov, S.; Koh, C.; Malone, W.; Lubbers, N.; Nebgen, B. Bond Order Predictions Using Deep Neural Networks. *J. Appl. Phys.* **2021**, *129*, No. 064701.

(5) Sifain, A. E.; Lubbers, N.; Nebgen, B. T.; Smith, J. S.; Lokhov, A. Y.; Isayev, O.; Roitberg, A. E.; Barros, K.; Tretiak, S. Discovering a Transferable Charge Assignment Model Using Machine Learning. *J. Phys. Chem. Lett.* **2018**, *9*, 4495−4501.

(6) Rupp, M.; Tkatchenko, A.; Müller, K.-R.; von Lilienfeld, O. A. Fast and Accurate Modeling of Molecular Atomization Energies with Machine Learning. *Phys. Rev. Lett.* **2012**, *108*, 058301.

(7) Hansen, K.; Montavon, G.; Biegler, F.; Fazli, S.; Rupp, M.; Scheffler, M.; von Lilienfeld, O. A.; Tkatchenko, A.; Müller, K.-R. Assessment and Validation of Machine Learning Methods for Predicting Molecular Atomization Energies. *J. Chem. Theory Comput.* **2013**, *9*, 3404−3419.

(8) Smith, J. S.; Nebgen, B. T.; Zubatyuk, R.; Lubbers, N.; Devereux, C.; Barros, K.; Tretiak, S.; Isayev, O.; Roitberg, A. E. Approaching Coupled Cluster Accuracy with a General-Purpose Neural Network Potential through Transfer Learning. *Nat. Commun.* **2019**, *10*, 2903.

(9) Montavon, G.; Rupp, M.; Gobre, V.; Vazquez-Mayagoitia, A.; Hansen, K.; Tkatchenko, A.; Müller, K.-R.; Anatole von Lilienfeld, O. Machine Learning of Molecular Electronic Properties in Chemical Compound Space. *New J. Phys.* **2013**, *15*, No. 095003.

(10) Li, Z.; Wang, S.; Chin, W. S.; Achenie, L. E.; Xin, H. High-Throughput Screening of Bimetallic Catalysts Enabled by Machine Learning. *J. Mater. Chem. A* **2017**, *5*, 24131−24138.

(11) Fung, V.; Hu, G.; Ganesh, P.; Sumpter, B. G. Machine Learned Features from Density of States for Accurate Adsorption Energy Prediction. *Nat. Commun.* **2021**, *12*, 88.

(12) Malone, W.; Kara, A. Predicting Adsorption Energies and the Physical Properties of H, N, and O Adsorbed on Transition Metal Surfaces: A Machine Learning Study. *Surf. Sci.* **2023**, *731*, No. 122252.

(13) Back, S.; Yoon, J.; Tian, N.; Zhong, W.; Tran, K.; Ulissi, Z. W. Convolutional Neural Network of Atomic Surface Structures to Predict Binding Energies for High-Throughput Screening of Catalysts. *J. Phys. Chem. Lett.* **2019**, *10*, 4401−4408.

(14) Mamun, O.; Winther, K. T.; Boes, J. R.; Bligaard, T. A Bayesian Framework for Adsorption Energy Prediction on Bimetallic Alloy Catalysts. *npj Comput. Mater.* **2020**, *6*, 177.

(15) Faber, F. A.; Christensen, A. S.; Huang, B.; von Lilienfeld, O. A. Alchemical and Structural Distribution Based Representation for Universal Quantum Machine Learning. *J. Chem. Phys.* **2018**, *148*, No. 241717.

(16) Marsault, M.; Sitja, G.; Henry, C. R. Regular Arrays of PD and AuPd Clusters on Ultrathin Alumina Films for Reactivity Studies. *Phys. Chem. Chem. Phys.* **2014**, *16*, 26458−26466.

(17) Hamm, G.; Becker, C.; Henry, C. R. Bimetallic PD−AU Nanocluster Arrays Grown on Nanostructured Alumina Templates. *Nanotechnology* **2006**, *17*, 1943−1947.

(18) Sitja, G.; Marsault, M.; Fré, N. A.; dé, N. A.; Leroy, r.; Sé, N. A.; Moal, verine L.; Henry, C. R. Regular Arrays of Palladium and Palladium-Gold Clusters Supported on Ultrathin Alumina Films: Stability under Oxygen. *Int. J. Nanotechnol.* **2012**, *9*, 567.

(19) Davis, R. J.; Boudart, M. Structure of Supported AuPd Clusters Determined by X-Ray Absorption Spectroscopy. *J. Phys. Chem. A* **1994**, *98*, 5471−5477.

(20) Yan, W.; Tang, Z.; Wang, L.; Wang, Q.; Yang, H.; Chen, S. AuPd Alloyed Clusters Supported by Carbon Nanosheets as Efficient Electrocatalysts for Oxygen Reduction. *Int. J. Hydrogen Energy* **2017**, *42*, 218−227.

(21) Shan, B.; Wang, L.; Yang, S.; Hyun, J.; Kapur, N.; Zhao, Y.; Nicholas, J. B.; Cho, K. First- Principles-Based Embedded Atom Method for AuPd Nanoparticles. *Phys. Rev. B* **2009**, *80*, 035404.

(22) Yildirim, H.; Kara, A.; Rahman, T. S. Tailoring Electronic Structure through Alloying: The AgnCu34−n (n = 0−34) Nanoparticle Family. *J. Phys. Chem. C* **2012**, *116*, 281−291.

(23) Zaman, N.; Lasri, K.; Lau, K. C.; Amine, K.; Kara, A. Computational Study of the Adsorption of Bimetallic Clusters on Alumina Substrate. *Surf. Sci.* **2020**, *700*, No. 121682.

(24) Beck, A.; Horváth, A.; Schay, Z.; Stefler, G.; Koppány, Z.; Sajó, I.; Geszti, O.; Guczi, L. Sol Derived Gold−Palladium Bimetallic Nanoparticles on TIO2: Structure and Catalytic Activity in CO Oxidation. *Top. Catal.* **2007**, *44*, 115−121.

(25) Maroun, F.; Ozanam, F.; Magnussen, O. M.; Behm, R. J. The Role of Atomic Ensembles in the Reactivity of Bimetallic Electrocatalysts. *Science* **2001**, *293*, 1811−1814.

(26) Han, Y.; Wang, J.; Kumar, D.; Yan, Z.; Goodman, D. A Kinetic Study of Vinyl Acetate Synthesis over PD-Based Catalysts: Kinetics of Vinyl Acetate Synthesis over PD−AU/SIO and Pd/SIO Catalysts. *J. Catal.* **2005**, *232*, 467−475.

(27) Pawelec, B.; Venezia, A. M.; La Parola, V.; Cano-Serrano, E.; Campos-Martin, J. M.; Fierro, J. L. G. AUPD Alloy Formation in Au-PD/al2o3 Catalysts and Its Role on Aromatics Hydrogenation. *Appl. Surf. Sci.* **2005**, *242*, 380−391.

(28) Venezia, A. M.; Parola, V. L.; Pawelec, B.; Fierro, J. L. G. Hydrogenation of Aromatics over Au-Pd/sio2-al2o3 Catalysts; Support Acidity Effect. *Appl. Catal. A Gen.* **2004**, *264*, 43−51.

(29) Baletto, F. Structural Properties of Sub-Nanometer Metallic Clusters. *J. Phys. Condens. Matter* **2019**, *31*, No. 113001.

(30) Michalewicz, Z.; Janikow, C. Z. Genetic Algorithms for Numerical Optimization. *Stat. Comput.* **1991**, *1*, 75−91.

(31) Deaven, D. M.; Ho, K. M. Molecular Geometry Optimization with a Genetic Algorithm. *Phys. Rev. Lett.* **1995**, *75*, 288−291.

(32) Paleico, M. L.; Behler, J. Global Optimization of Copper Clusters at the Zno(10$\bar{1}$0) Surface Using a DFT-Based Neural Network Potential and Genetic Algorithms. *J. Chem. Phys.* **2020**, *153*, No. 054704.

(33) Kolsbjerg, E. L.; Peterson, A. A.; Hammer, B. Neural-Network-Enhanced Evolutionary Algorithm Applied to Supported Metal Nanoparticles. *Phys. Rev. B* **2018**, *97*, 195424.

(34) Jennings, P. C.; Lysgaard, S.; Hummelshøj, J. S.; Vegge, T.; Bligaard, T. Genetic Algorithms for Computational Materials Discovery Accelerated by Machine Learning. *npj Comput. Mater.* **2019**, *5*, 46.

(35) Heydariyan, S.; Nouri, M. R.; Alaei, M.; Allahyari, Z.; Niehaus, T. A. New Candidates for the Global Minimum of Medium-Sized Silicon Clusters: A Hybrid DFTB/DFT Genetic Algorithm Applied to Sin, n = 8−80. *J. Chem. Phys.* **2018**, *149*, No. 074313.

(36) Darby, S.; Mortimer-Jones, T. V.; Johnston, R. L.; Roberts, C. Theoretical Study of Cu−Au Nanoalloy Clusters Using a Genetic Algorithm. *J. Chem. Phys.* **2002**, *116*, 1536−1550.

(37) Kelting, R.; Otterstätter, R.; Weis, P.; Drebov, N.; Ahlrichs, R.; Kappes, M. M. Structures and Energetics of Small Lead Cluster Ions. *J. Chem. Phys.* **2011**, *134*, No. 024311.

(38) Kelting, R.; Baldes, A.; Schwarz, U.; Rapps, T.; Schooss, D.; Weis, P.; Neiss, C.; Weigend, F.; Kappes, M. M. Structures of Small Bismuth Cluster Cations. *J. Chem. Phys.* **2012**, *136*, No. 154309.

(39) Jia, J. M.; Chen, G. B.; Shi, D. N.; Wang, B. L. Structural and Electronic Properties of Bin (N = 2−14) Clusters from Density-Functional Calculations. *Eur. Phys. J. D* **2008**, *47*, 359−365.

(40) Seifried, C.; Longo, L.; Pollak, P.; Weigend, F. The Chemical Space of PBN−nBin and (PbN−nBin)+: A Systematic Study for n = 3−13. *J. Chem. Phys.* **2017**, *146*, No. 034304.

(41) Weigend, F.; Schrodt, C.; Ahlrichs, R. Atom Distributions in Binary Atom Clusters: A Perturbational Approach and Its Validation in a Case Study. *J. Chem. Phys.* **2004**, *121*, 10380−10384.

(42) von Lilienfeld, O. A.; Lins, R. D.; Rothlisberger, U. Variational Particle Number Approach for Rational Compound Design. *Phys. Rev. Lett.* **2005**, *95*, 153002.

(43) Balawender, R.; Welearegay, M. A.; Lesiuk, M.; De Proft, F.; Geerlings, P. Exploring Chemical Space with the Alchemical Derivatives. *J. Chem. Theory Comput.* **2013**, *9*, 5327−5340.

(44) Bozkurt, E.; Perez, M. A.; Hovius, R.; Browning, N. J.; Rothlisberger, U. Genetic Algorithm Based Design and Experimental Characterization of a Highly Thermostable Metalloprotein. *J. Am. Chem. Soc.* **2018**, *140*, 4517−4521.

(45) Patra, T. K.; Meenakshisundaram, V.; Hung, J.-H.; Simmons, D. S. Neural-Network-Biased Genetic Algorithms for Materials Design: Evolutionary Algorithms That Learn. *ACS Comb. Sci.* **2017**, *19*, 96−107.

(46) Kolsbjerg, E. L.; Peterson, A. A.; Hammer, B. Neural-Network-Enhanced Evolutionary Algorithm Applied to Supported Metal Nanoparticles. *Phys. Rev. B* **2018**, *97*, 195424.

(47) Jennings, P. C.; Lysgaard, S.; Hummelshøj, J. S.; Vegge, T.; Bligaard, T. Genetic Algorithms for Computational Materials Discovery Accelerated by Machine Learning. *npj Comput. Mater.* **2019**, *5*, 46.

(48) Jensen, P. B.; Lysgaard, S.; Quaade, U. J.; Vegge, T. Designing Mixed Metal Halide Ammines for Ammonia Storage Using Density Functional Theory and Genetic Algorithms. *Phys. Chem. Chem. Phys.* **2014**, *16*, 19732−19740.

(49) Heydariyan, S.; Nouri, M. R.; Alaei, M.; Allahyari, Z.; Niehaus, T. A. New Candidates for the Global Minimum of Medium-Sized Silicon Clusters: A Hybrid DFTB/DFT Genetic Algorithm Applied to Sin, n = 8−80. *J. Chem. Phys.* **2018**, *149*, No. 074313.

(50) Buendía, F.; Vargas, J. A.; Johnston, R. L.; Beltrán, M. R. Study of the Stability of Small AURH Clusters Found by a Genetic Algorithm Methodology. *Comput. Theor. Chem.* **2017**, *1119*, 51−58.

(51) Larsen, A.; Castelli, I.; Groves, M.; Jennings, P.; Kolsbjerg, E.; Lysgaard, S.; Pastewka, L.; Schütt, O.; Vilhelmsen, L.; Mortensen, J.; Christensen, R.; Hammer, B.; Jensen, P.; Kubal, J.; Maronsson, J.; Peterson, A.; Strange, M.; Walter, M.; Blomqvist, J.; Dułak, M.; Hargus, C.; Kermode, J.; Kaasbjerg, K.; Maxson, T.; Rostgaard, C.; Thygesen, K.; Zeng, Z.; Friis, J.; Hermes, E.; Kitchin, J.; Olsen, T.; Schiøtz, J.; Vegge, T.; Jacobsen, K. The Atomic Simulation Environment—A Python library for working with atoms. *J. Phys.: Condens. Matter* **2017**, *29*, No. 273002.

(52) Schütt, K. T.; Kessel, P.; Gastegger, M.; Nicoli, K. A.; Tkatchenko, A.; Müller, K.-R. Schnetpack: A Deep Learning Toolbox for Atomistic Systems. *J. Chem. Theory Comput.* **2019**, *15*, 448−455.

(53) NVIDIA; Vingelmann, P.; Fitzek, F. H. P.. *CUDA, Release: 10.2.89*; 2020.

(54) Kresse, G.; Hafner, J. Ab Initio Molecular Dynamics for Liquid Metals. *Phys. Rev. B* **1993**, *47*, 558−561.

(55) Kresse, G.; Furthmüller, J. Efficiency of AB-Initio Total Energy Calculations for Metals and Semiconductors Using a Plane-Wave Basis Set. *Comput. Mater. Sci.* **1996**, *6*, 15−50.

(56) Kresse, G.; Furthmüller, J. Efficient Iterative Schemes forAb InitioTotal-Energy Calculations Using a Plane-Wave Basis Set. *Phys. Rev. B* **1996**, *54*, 11169−11186.

(57) Perdew, J. P.; Burke, K.; Ernzerhof, M. Generalized Gradient Approximation Made Simple. *Phys. Rev. Lett.* **1996**, *77*, 3865−3868.

(58) Blöchl, P. E. Projector Augmented-Wave Method. *Phys. Rev. B* **1994**, *50*, 17953−17979.

https://doi.org/10.1021/acs.jcim.3c00609
J. Chem. Inf. Model. 2023, 63, 5045−5055